Available online at www.sciencedirect.com

ScienceDirect

Procedia Structural Integrity 18 (2019) 671–687

Structural Integrity Procedia

www.elsevier.com/locate/procedia

25th International Conference on Fracture and Structural Integrity

Modeling the influence of stress triaxiality on the failure strain of nodular cast iron microstructures

L. Collini*, F. Moroni, A. Pirondi

Department of Engineering and Architecture, University of Parma
Viale delle Scienze 181/A, 43124 Parma (Italy)

Abstract

In this study the fracture behavior of different cast iron microstructures subjected to tensile loading under different triaxialities is simulated by a finite element, 3-D Reference Volume Element approach. Three ferritic/pearlitic heterogeneous matrixes are considered which are representative of the class material grades for strength and ductility. Isotropic ductile and shear damage models are considered for the matrix constituents as concurrent damage mechanisms at the microscale, while graphite nodules are considered as voids acting as stress concentrators. Numerical results confirm experimental findings about local strain distribution and damage accumulation, and reproduce the engineering macroscopic behavior. The stress triaxiality is found to play a strong effect on the failure strain, extending the potentialities of this RVE modeling approach.

Peer-review under responsibility of the Gruppo Italiano Frattura (IGF) ExCo.

Keywords: Ductile cast iron; RVE; ductile damage model; shear damage model; triaxilaity.

1. Background and motivation

The variety of industrial applications of ductile cast irons (DCI) indicates that this class of materials is still attractive due to performances, machinability and formability, and overall cost benefits. Nodular or spheroidal DCI due their large use also to the large set of properties offered, that are directly related to the ferritic/pearlitic microstructure, Davis (1996), and that range from very ductile and high impact toughness grades, i.e. the EN-GJS-350, to high strength and hardness grades, as the EN-GJS-900.

* Corresponding author. Tel.: +30-0521-905892; fax: +39-0521-905705.
E-mail address: luca.collini@unipr.it

2452-3216
Peer-review under responsibility of the Gruppo Italiano Frattura (IGF) ExCo.
10.1016/j.prostr.2019.08.215

Nomenclature

a	Mean half interparticle spacing
ψ_G	graphite volume fraction
ψ_F	ferrite volume fraction
N	nodule count
d_G	nodule average diameter
K_{ti}	elastic stress concentration factor along the i-direction, i = 1, 2, 3
σ^0	yield stress
A, B	parameters of Johnson-Cook hardening law
n	hardening exponent
K_i	parameters of ductile damage model, i = 1, 2, 3
p	first stress invariant (hydrostatic pressure)
q	second stress invariant (equal to von Mises equivalent stress, σ_{eq})
η	local stress triaxiality inside the RVE (η = $-p/q$)
$\bar{\varepsilon}_D^{pl}$	equivalent plastic strain at the onset of damage in ductile criterion
$\bar{\varepsilon}_S^{pl}$	equivalent plastic strain at the onset of damage in shear criterion
$\bar{\varepsilon}_f^{pl}$	equivalent strain at failure
θ_S	shear stress ratio
k_s	material shear damage parameter
ω_D, D	damage variables
l	RVE size
L_{EL}	Finite element characteristic length
c	index of particle clustering
Σ_{ij}	stresses at the meso-scale
T	stress triaxiality at the meso-scale
E_f^{pl}	RVE failure strain
Υ_f^{pl}	RVE failure displacement

Since many decades, the DCI peculiar structure motivated the study of plasticity and damage, with the aim of optimizing the material performance and of calibrating a relatively new class of material damage models. Experimental studies have been done at the macroscopic level to relate microstructural features on ductility and static or fatigue strength, see for example Bradley et al. (1990), Tartaglia et al. (2000), Hafiz (2001), Nicoletto et al. (2002), Collini et al. (2005), Gonzaga et al. (2009), Lacaze et al. (2016). Here, the matrix composition, heat treatment and graphite shape and spacing, are correlated to the desired mechanical properties. On the simulation side instead, starting from the work by Needleman (1987, 1991), DCI structure served as field for the development of new plasticity-based models of damage, in which strain localization phenomena are induced by the inherent stress concentrators, i.e. the graphite nodule cavities, and failure occurs for the nucleation, growth and coalescence of those cavities. A comprehensive review of the modeling strategies can be found in Hütter et al., 2015. The interaction between closely spaced particles on the kinetics of the damage mechanism is also studied, see for example Guillermer-Neel et al. (2000), and an attempt is made to define quantitative parameters accounting for the free path between the nodules, or by applying a critical void volume fraction concept. We can group these approaches into “simulation of the behavior at the micro- to mesoscopic scale”.

Nevertheless, not all the observable phenomena are fully understood yet. For example, peculiar configurations of the heterogeneous microstructure makes it possible to find a brittle fracture of the ductile phase, and, conversely, markers of ductile failure in the brittle constituent, see Yanagisawa et al. (1983), Nicoletto et al. (2002). Nodules interaction, particular morphology of grains or uneven concentration of chemical elements (Mn and Si) can be

responsible of such local behavior, but the reason still is unclear. Also residual stresses, resulting from the cooling down to room temperature, have been demonstrated to be critical for an accurate prediction of the non-linear behavior of the DCI in the early deformation range, Bonora and Ruggiero (2005).

In this work, the damage mechanism of DCI is modeled by a RVE approach introducing two main novelties: (i) the simultaneous damage and failure of both ferritic and pearlitic matrix phases, that are described by distinct damage models, and (ii) the application on the RVE of different values of triaxiality, which has been demonstrated to strongly influence the fracture of ductile metals. Random arrangements of graphite nodule cavities are reproduced inside the RVE and periodic boundary conditions are applied. Plasticity rules and the damage evolution laws are given to the matrix constituents at the microscale, while different triaxialities are imposed at the RVE boundaries on the mesoscale. In this way, the *engineering* behavior of the material is deduced by analyzing the RVE as a homogeneous medium, and the damage micromechanisms are studied moving back to the microscale. Triaxiality effect is analyzed because different triaxiality states are found very commonly in the industrial application, for example in proximity of a notch, which concentrates the stresses and tends to create higher triaxialities. Results will show that different stress triaxiality very strongly influences the DCI failure strain.

This work is then devoted to the deeper understanding of the damage mechanism in this class of materials under different loading conditions, and of its influence on the response measurable by classical mechanical testing. However, it is also a comprehensive exploration of the possibilities and limitations given by modern calculation tools: on one hand obtainable results indicate an extraordinary reproducibility of mechanism of real microstructures. Conversely, a strong dependence from accuracy of modeling and tuning of parameters is proven.

2. Damage and failure of ductile cast iron

2.1. Ambiguous damage mechanisms

Fracture and fracture toughness of DCI manly depend from the matrix structure, Bradley et al. (1990). Under monotonic tension loading ductile iron shows no distinct yield point, and no tension–compression symmetry, with the yield stress in compression being larger than in tension up to 7%, Hütter et al. (2015). The strength and the hardening behavior are strongly influenced by the matrix material properties showing a ratio of yield stress to ultimate strength of about 0.65-0.75. In ferritic–pearlitic structures, the yield stress increases also with increasing content of pearlite and increasing contents of Silicon. Also, it has been found that the strain to fracture depends strongly on the microstructure and chemical composition. With higher content of pearlite, and/or stronger deviations of the shape of the graphite particles from the spherical one, and/or higher contents of Silicon the material becomes more brittle and thus the strain at failure decreases. Empirical relations for the effect were also derived.

However, especially under low stress triaxialities the graphite plays an important role, which is investigated only in a few studies yet, Memhard et al. (2011), Dahlberg et al. (2014). Regarding fracture testing, “general consensus of the criteria for crack initiation has not been reached yet”, because of the inhomogeneous microstructure, Kobayashi (2004).

The influence of the microstructure of the matrix on the fracture toughness was investigated intensively, and generally it is found that higher content of pearlite leads to higher strength at the expense of lower fracture toughness values. However, it has to be pointed out that in ferritic/pearlitic DCI, due to the presence of nodule cavities and peculiar phase morphology, the damage mechanism is not uniquely definite. Ferrite represents the ductile phase, which is supposed to fail following ductile mechanisms; pearlite, which is composed by lamellar structure of ferrite and cementite, generally shows a brittle or quasi-brittle behavior, see as example Fig. 1(a). Each nodule acts as a void that subsequently grows with strain. Coalescence with neighboring voids results in ridges that outline large equiaxed dimples: voids that are about one order of magnitude smaller than the primary dimples are typically observed at the boundaries of the larger dimples and are found at the ridges of the primary voids, Kuna et al. (1996), Ghahremaninezhad et al. (2012), D’Agostino et al. (2017).

Tensile and fracture toughness tests demonstrate this general behavior, but exceptions do exist. In pearlitic DCI microstructures, the ferrite capsules surrounding graphite nodules can show cleavage facets typical of ferrous alloys, as illustrated in Fig. 1(b), taken from Nicoletto et al. (2002, 2004, 2006). Iacoviello et al. (2013) report “cleavage in ferritic shields around the graphite nodules” and, analogously to the pearlitic, “striations” mainly due to transgranular

damaging mechanism of pearlitic lamellae. It was concluded that initially the nodules create voids that grow by plastic flow, but this is terminated by a transition to deformation in a very localized region over which coalescence occurs either by the formation of void sheets or through cleavage, Gonzaga et al. (2009).

Conversely, for highly ferritic microstructures, under specific conditions, entrapped pearlitic areas can exhibit ductile fracture with fine dimples as shown in Fig. 1(c), which is detailed in Fig. 1(d). In investigated pearlitic steels, the fracture mechanism is found to be a ductile/brittle competition driven by different promoters, i.e. microvoids in the ductile phase (lamellar ferrite), microcracks in the brittle phase (cementite lamellae), and interfacial microcracks, Peng et al. (2004). In these cases of fully pearlitic structure, microstructural parameters, as the pearlite interlamellar spacing, are related to the fracture mechanism, Lewandowski et al. (1986).

2.2. Role of graphite nodules and triaxiality effects

In ductile metals, for a given stress state, the deviatoric component causes plastic deformation, whereas the hydrostatic component affects ductility. Then, the overall deformation and fracture behavior can be described by a triaxiality ratio, which is defined as the ratio of hydrostatic stress over von Mises equivalent stress. The higher the triaxiality ratio, the lower the ductility, Mirza et al. (1996).

According to Lin et al. (1994), the failure mode in ferritic DCI changes from pure dimple to a mixed mode of dimple and cleavage when the nodule spacing increases over a certain value. At the same time, experiments show that the higher the local triaxiality, the lower the ductility and the larger the chances for cleavage fracture to occur.

A model to estimate the local triaxiality as a function of nodule spacing of ferritic iron under uniaxial tension was previously proposed by Yanagisawa and Lui (1983), assuming graphite nodules as voids. The model hypotheses that the triaxiality ratio at the center region of the ferrite matrix is:

$$\eta = 1/3 + a/d_G \tag{1}$$

where a is the half interparticle spacing of the nodules and d_G the average diameter. In accordance with this model, bigger and closer nodules minimize the triaxiality promoting the ductility and ductile mechanism of fracture, small and distant nodules decrease the ductility and facilitate the cleavage fracture.

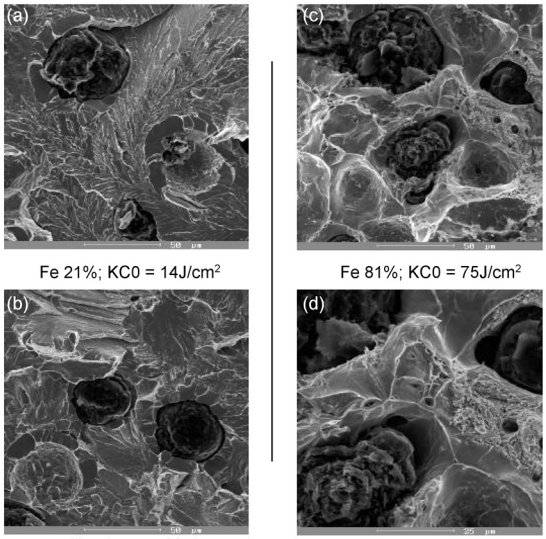

Fig. 1. (a) transcrystalline continuous cleavage of pearlite; (b) transcrystalline continuous cleavage of ferrite capsules; (c) transcrystalline ductile fracture of ferrite; (d) detail of (c), transcrystalline ductile fracture of pearlite with fine dimples. From Nicoletto et al., (2002).

However, the model does not consider another important effect, which is the stress concentration near the graphite nodules, and consider a ferritic matrix only. By changing nodule spacing and nodule shape simultaneously, Chao et al. (1988) took an additional step toward the investigation of the shape effect on triaxiality ratio. Anyway, systematic experimental data of varying separately the individual graphite nodule variables need to be provided.

3. Considered microstructures

Three microstructures are here taken into consideration, the full ferritic M1, and two ferritic/pearlitic mixed structures, M2 and M3. These are shown in the micrographs of Fig. 2 with the same scale. As indicated in Tab. 1, the chemical composition of the three ductile irons only differ in the Silicon and Phosphor content, which varies the Equivalent Carbon content CE[1] and facilitate the formation of desired structure. Tab. 2 reports the microstructural and strength data: graphite volume content decreases with the increasing of pearlite formation, and spheroids get thinner, more numerous and closer to each other. Ferrite grains get smaller in average dimension with increasing of graphite content. However, static strength and ductility mostly depends on the ferrite/pearlite ratio: yield strength, ultimate strength and hardness increases with pearlite content, ductility decreases as indicated by the impact fracture toughness data KC0.

These microstructures are considered as representative of the wider class of ductile irons, since they contain the most meaningful features. It's important to notice that a 100% pearlitic structure is almost impossible to obtain, for the carbon absorption from the matrix in the proximity of the inoculated graphite nodules. In these areas, a typical *bull's eye* structure of ferritic enclosing the spheroids is commonly found.

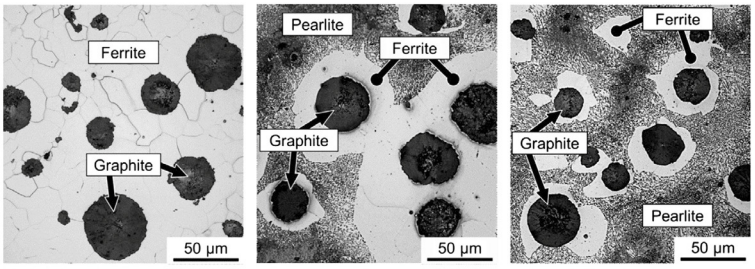

Fig. 2. Typical classes of ductile cast iron microstructures, from Endo et al. (2014).

Table 1. Chemistry data of cast iron melts, from Nicoletto et al. (2002).

Melt No.	C	S	P	Si	Mn	Cr	Ni	Mo	Al	Cu	Mg	Ti	Ce	Sn	CE
M1	3,69	0,010	0,063	3,10	0,26	0,04	-	-	-	-	0,046	-	-	-	4,74
M2	3,68	0,013	0,012	2,38	0,26	0,04	0,03	0,01	0,022	0,44	0,039	<0,005	0,0028	0,006	4,48
M3	3,65	0,016	0,019	2,18	0,23	0,09	0,05	0,01	0,034	0,40	0,044	0,007	0,0056	<0,005	4,38

Table 2. Mechanical properties of considered cast iron microstructures, from Nicoletto et al. (2002).

Melt No.	Graphite form	N (mm^{-1})	ψ_G (%)	ψ_F (%)	E (GPa)	σ^0 (MPa)	σ^u (MPa)	$\varepsilon^{pl}{}_f$ (%)	KC0 (J/cm^2)	HB
M1	80%VI7+20%V7	174	15.0	93.5	162	350	535	15	90	178
M2	70%VI6+30%V6	187	12.4	50.7	170	368	611	12.3	30÷40	189
M3	70%VI5+30%V7	196	9.9	16,0	169	419	745	7.6	8÷11	236

[1] For cast iron the equivalent carbon content (CE) concept is used to understand how alloying elements will affect the heat treatment and casting behavior. CE = %C + 0.33 (%Si + %P).

4. Modeling approach

4.1. RVE generation and boundary conditions

Due to the peculiar DCI microstructure, in this study a RVE approach is chosen, for the effective properties are efficiently derived from the knowledge of the constitutive laws and spatial distribution of the constituents. The RVE is a "small" volume statistically representative of the bulk material, for it contains any peculiar element at the microstructural level, and it should be as small as possible in order to reduce the calculation time, Collini (2010), Kanita et al. (2003). Residual stress at the microscale due to cooling are not accounted for in order to keep the model as simple as possible.

This approach has been already tried for the DCI material system, with the aim of obtaining macro-behavior from micro-characteristics of the constituents and of studying the damage mechanisms, see for example Steglich et al. (1997), Bonora et al. (2005), Collini et al. (2005), Nicoletto et al. (2006), Hütter et al. (2015), Andriollo et al. (2019), or again for calibrating GTN-like models, as in Kuna et al. (1996), and Tvergaard (1996). As already stated in the introduction, the novelty of the present work is to consider a real spatial distribution of graphite nodules inserted in a realistic dual-phase matrix. Then, for each considered iron class, a cubic RVE of size l = 0.250 mm is defined containing random configurations of voids. For this purpose, it is used the open-source toolbox Mote3D developed by Richter (2017), which automatically creates overlapping or non-overlapping spherical particles with user-defined minimum inter-particle, centre-to-centre distance and periodic boundary. The RVEs, shown in Fig. 3, reflect all the characteristic statistical parameters of Tab. 2 derived from metallographic sections as the nodule counting, average diameter, standard deviation and clustering. Details of the assumed data are indicated in Tab. 3.

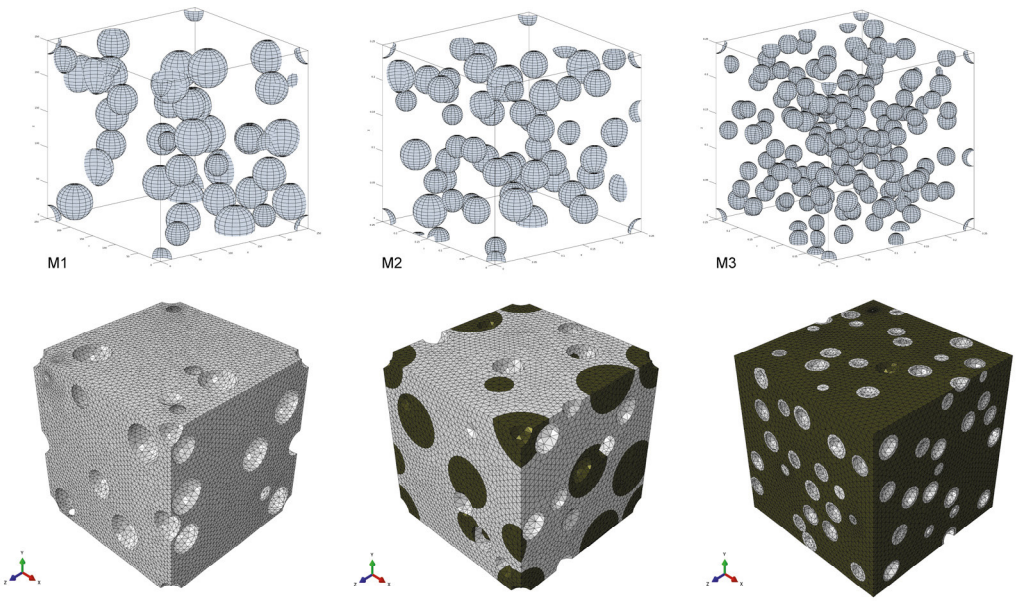

Fig. 3. RVE of ductile iron microstructures as generated and meshed; ferrite and pearlite are colored.

Table 3. Microstructural modeling features.

RVE	N	d_G (μm)	c	Nodes	Elements	Element type	DOF	L_{EL} (mm)
M1	49	45 ± 8	1	46,067	204,456	C3D4	138,201	0.01105
M2	67	38 ± 5	1.2	50,394	268,181	C3D4	161,403	0.01054
M3	189	25 ± 2	1.4	53,050	255,627	C3D4	159,156	0.01104

Regarding the volume size, a bias in the estimation of the effective properties is observed for too small volumes for all types of boundary conditions. The variance of computed apparent properties for each volume size is then used to define the precision of the estimation introducing the key-notion of integral range to relate this error estimation and the definition of the RVE size. For given desired precision and number of microstructural arrangements, one is able to provide a minimal volume size for the computation of effective properties, or, conversely, the results can be used to predict the minimal number of realizations that must be considered for a given volume size in order to estimate the effective property for a given precision. The RVE sizes for this work are qualitatively defined in such a way at least 3 nodule-to-nodule free paths can lay in a side, considering the full ferritic structure. This size is then kept for the other microstructures. The verification of RVE response is then carried out considering the anisotropy of elastic properties, which should fall within an arbitrary deviation value as shown in the result section.

Regarding the graphite nodules, in this work they are considered spherical voids, even if on this argument the literature is variegated. Some studies consider the role of graphite nodules on matrix damage mechanism as negligible, see Dong et al. (1997), Steglich et al. (1997), Zhang et al. (1999), Berdin et al. (2001) Ghahremaninezhad et al. (2012), Zybell et al. (2014), Kuna et al. (2016); but some other identify a possible active role of graphite at the local level, for example Di Cocco et al. (2013). However, the nodules' role as toughening particles is weakened at high triaxiality states, Di Cocco et al. (2014), or depends not uniquely on the matrix structure, Iacoviello et al. (2008).

The microstructures generated are imported in the Abaqus™ CAE model by Python-based scripts. Finite element simulations are then performed imposing a homogeneous stress or strain field under periodic boundary conditions. For this purpose, Abaqus™ provides the powerful functionality of a Micromechanics plugin developed by Omairey et al. (2019), for setting up and post-processing RVE models, including the application of far-field loading through periodic or non-periodic boundary conditions. These latter assume that the solution field φ (in this case the displacement u_i) exhibits the following form:

$$\varphi\left(x_j + p_j^{\alpha}\right) = \varphi\left(x_j\right) + \left\langle \frac{\partial \varphi}{\partial x} \right\rangle p_j^{\alpha} \tag{2}$$

where x_j is the coordinate, p_j^{α} is the α^{th} vector of periodicity, and $\left\langle \frac{\partial \varphi}{\partial x} \right\rangle$ is the far-field gradient of the solution field (i.e., the far-field displacement gradient). Operatively, the plugin imposes this relationship on the boundary nodes of the RVE through the use of equation constraints. The far-field gradient is introduced through the degrees of freedom of assembly-level nodes, called far-field reference nodes, which are added to the analysis and are not attached to any elements. The far-field gradient can be specified by applying boundary conditions to these far-field reference nodes, such as, for the case of the present study, uniform traction or uniform displacement. The plugin post processing includes the calculation of the RVE homogenized properties from the completed analysis as well as performing averaging and statistical analysis of the fields in the whole volume and within individual constituents.

The control of the stress triaxiality over the cell is crucial, Lin et al. (2006). In this work, it is made on the meso-scale of the RVEs, imposing the meso-stresses Σ_{ij} according to the general definition of triaxiality T:

$$T = \frac{\Sigma_m}{\Sigma_{eq}} = \frac{\frac{1}{3}\left(\Sigma_{11} + \Sigma_{22} + \Sigma_{33}\right)}{\frac{1}{\sqrt{2}}\sqrt{\left(\Sigma_{11} - \Sigma_{22}\right)^2 + \left(\Sigma_{22} - \Sigma_{33}\right)^2 + \left(\Sigma_{11} - \Sigma_{33}\right)^2}} \tag{3}$$

In this study the triaxiality values of Tab. 4 are considered and imposed by imposing uniform tractions Σ_{ij} at the boundaries. The RVE failure strain E_f^{pl} is then determined as the maximum displacement $\Upsilon_{f,j}^{pl}$ along the direction j reached by the simulation before degradation, relative to the cell dimension l_j and under the triaxiality T_i, Eq. (4):

$$\mathrm{E}_f^{pl}\Big|_{T_i} = \frac{\Upsilon_{f,ij}^{pl}}{I_j} \tag{4}$$

Table 4. Triaxiality ratios imposed on the RVE at the meso-scale.

T	Σ_{11}	Σ_{22}	Σ_{33}
-0.333	-1	0	0
-0.126	-1	0.5	0
0.000	1	-1	0
0.126	1	-1/2	0
0.218	1	-1/4	0
0.333	1	0	0
0.577	1	1/2	0
1.000	1	1	1/4
1.667	1	1/2	1

4.2. Plastic flow

In this work a classical plasticity model is chosen to reproduce the plastic flow of the two phases. Isotropic hardening with a Mises-type yield surface, associated flow rule and a Johnson-Cook hardening law is used, where the yield stress, σ^0, is assumed to be of the form:

$$\sigma^0 = \left[A + B\left(\bar{\varepsilon}^{pl}\right)^n \right]\left(1-\hat{\theta}^m\right) \tag{5}$$

The parameters *A, B* and the hardening exponent *n* are taken from the literature for a α-ferrite Fe-Si matrix, Springer (2012), and for fine pearlite structure, Hyzak et al. (1976), Gensamer et al. (2012), Toribio et al. (2016). The values are reported in Tab. 5 and in a graphical form in Fig. 4. Since neither strain rate nor temperature dependence are considered, the related parameters are set to zero.

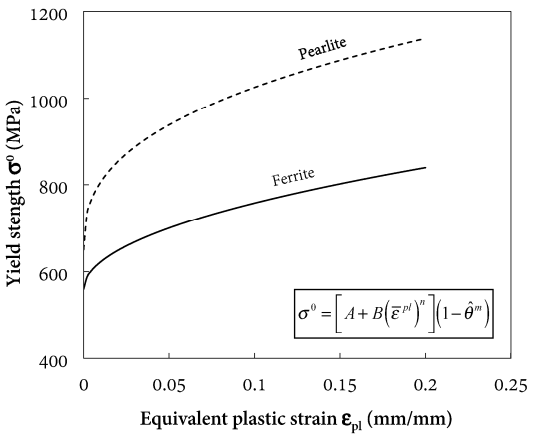

Fig. 4. Model of plastic flow for the matrix constituents.

4.3. Ferrite damage

The damage of the ferrite phase is here modeled with the Abaqus™ ductile damage, which is a phenomenological model for predicting the onset of damage due to nucleation, growth, and coalescence of voids. The model assumes that the equivalent plastic strain at the onset of damage $\bar{\varepsilon}_D^{pl} = f\left(\eta, \dot{\varepsilon}_D^{pl}\right)$ is a function of the stress triaxiality and strain rate, where $\eta = -p/q$ is the local stress triaxiality with p the hydrostatic pressure and q the deviatoric stress at the micro-scale. The damage initiation is satisfied when:

$$\omega_D = \int \frac{d\bar{\varepsilon}^{pl}}{\bar{\varepsilon}_D^{pl}\left(\eta, \dot{\varepsilon}_D^{pl}\right)} = 1 \tag{6}$$

where ω_D is a state variable that increases monotonically as $\Delta\omega_D$ increases with the plastic deformation for each increment of plastic strain $\Delta\bar{\varepsilon}_D^{pl}$. In this study, for the ferritic phase the fracture strain vs. stress triaxiality dependence is assumed to be an exponential law of the Johnson-Cook type:

$$\varepsilon_D^{pl} = \mathrm{K}_1 + \mathrm{K}_2\, \mathrm{e}^{-\mathrm{K}_3 \eta} \tag{7}$$

The parameters in Eq. (7) are reported in Tab. 5, and the represented in graphical form is depicted in Fig. 5. This assumption is supported by behavior of α-ferrite and ferritic steels observed in experimental tests under variable triaxiality conditions, Hancock et al. (1976), Johnson et al. (1985), Mirza et al. (1996), Maresca (1997), Hopperstad et al. (2003), Bao et al. (2004, 2009), Ohata et al. (2008), Springer (2012), Cheng et al. (2017), Hradil et al. (2017). For negative stress triaxiality values, if no data are available no dependency is assumed and failure strain is kept constant, Manjoine (1982).

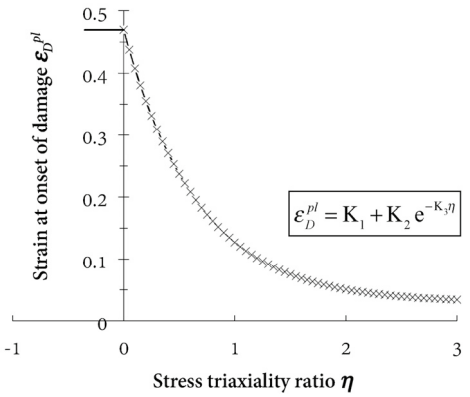

Fig. 5. Equivalent strain at the onset of damage of ferrite.

Once the initiation criterion of Eq. (6) is satisfied, the material stiffness is progressively degraded by the FE analysis according to a specified damage evolution law for the criterion, having effect on the material response and eventually leading to the material failure. Here, in conjunction with the ductile damage model Abaqus™ assumes that the degradation of the stiffness follows a scalar damage variable, and at any given time during the analysis the stress tensor in the material is given by the scalar damage equation:

$$\boldsymbol{\sigma} = \left(1 - D\right)\bar{\boldsymbol{\sigma}} \tag{8}$$

where D is the overall damage variable and $\boldsymbol{s}$ is the effective (or undamaged) stress tensor computed in the current increment. The material looses its load-carrying capacity when $D = 1$, as illustrated in the scheme of Fig. 6.

In the calculation, any element is removed from the mesh if all of the section points at any one integration location have lost their load-carrying capacity. The plastic displacement measure $\dot{\bar{u}}^{pl}$ (which is mesh-dependent from the element characteristic length L_{EL}, $\dot{\bar{u}}^{pl} = L_{EL}\dot{\bar{\varepsilon}}^{pl}$) is used to drive the evolution of damage after damage initiation, with the values reported in Tab. 5. In order to reproduce a hard damage evolution, the exponential softening type and the maximum degradation option are set, with exponent α equal to 10. The option of removing of elements from the mesh is also employed when the damage variable is equal to 0.95.

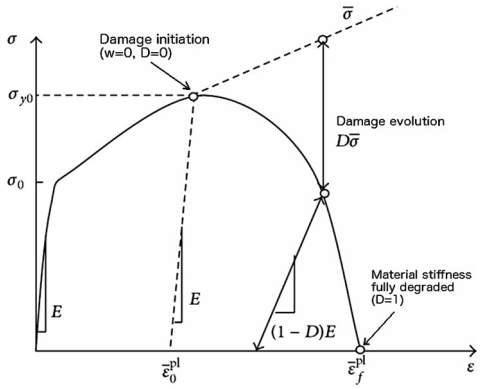

Fig. 6. Scheme of progressive damage degradation.

Table 5. Parameters of material models.

Phase	ρ (kg/mm^3)	E (GPa)	ν	Plastic flow parameters				Ductile/shear damage				Damage evolution	
				A (MPa)	B (MPa)	n	m	K_1	K_2	K_3	k_S	$\bar{u}_f^{pl}$	α
Ferrite	7,85e-6	206	0.3	560	625	0.50	0	0.029	0.44	-1.5	–	0.0015	10
Pearlite	7,85e-6	203	0.3	650	900	0.38	0	–	–	–	0.5	0.0004	10

4.4. Pearlite damage

Modeling of the fracture behavior of the pearlitic phase is somehow more controversial. As already reported in the introduction, Peng et al. (2004) indicate as in pearlitic steels the fracture mechanism is a ductile/brittle competition driven by different promoters, i.e. microvoids in the ductile phase, microcracks in the brittle phase, and interfacial microcracks. A damage evolution law corresponding to different patterns of microdefects is then formulated, containing explicitly the interlamellar spacing, which is regarded as one of the most important microstructure parameters for the material.

Other observations too, Toribio et al. (2016), Hohenwarter et al. (2017), Nemoto et al. (2017), evidence a strong dependency from the cementite/ferrite structure morphology, which constitutes the pearlite structure. Cementite is growing in colonies that can be coarse of finer. In the case of relatively fine, pearlite microcracks with uneven appearance and shorter in length than the colony size are observed, indicating a ductile fracture behavior. On the other hand, in the case of relatively coarse pearlite (wider interlamellar spacing and greater colonies), the inclined cracking is generally of greater length (even across the complete colony) and looks more uniform; as a consequence, the fracture behavior in this case is more brittle. Therefore, the fracture process is determined by physical events in the pearlite colony with the lamellae being parallel to the tensile axis, where the deformation occurs in narrow bands of locally intense shear stress according to the Miller–Smith mechanism, Miller et al. (1970), Dollar et al. (1988). In this phenomenon, the slip bands in the ferrite produce microcracking in the cementite plates, followed by tearing in the ferrite lamellae, as the scheme of Fig. 7 tries to illustrates, Toribio et al. (2016).

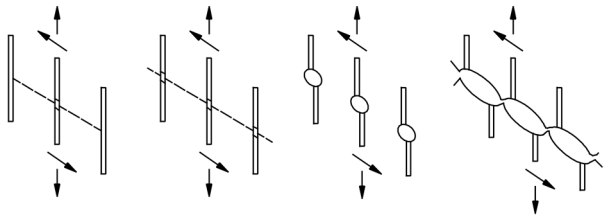

Fig. 7. Scheme of the Miller-Smith mechanism of void nucleation growth and coalescence after shear bands interaction in pearlite, Toribio et al. (2016).

This combined, orientation-dependent mechanism, could reasonably explain the experimental findings of some fracture surfaces in pearlite, as shown in section 3. In particular, the shear mechanism of ductile phase can be pointed as initial microcrack promoter of cementite. For this reason, the shear criterion available in Abaqus™ code is chosen to model the fracture behavior of pearlite in DCI, in conjunction with lower yield point and hardening with respect to ferrite. The Abaqus™ shear criterion is a phenomenological model for predicting the onset of damage due to local shear band localization, and assumes that the equivalent plastic strain at the onset of damage, $\bar{\varepsilon}_S^{pl}$, is a function of the shear stress ratio (and strain rate, where necessary), $\bar{\varepsilon}_S^{pl} = f\left(\theta_S, \dot{\bar{\varepsilon}}^{pl}\right)$, being the shear stress ratio defined as:

$$\theta_S = \frac{q + k_S p}{\tau_{\max}} = \frac{\left(1 - k_S \eta\right)\sigma_{eq}}{\tau_{\max}} \tag{9}$$

where k_s is a material parameter that consider the influence of local hydrostatic stress p. A typical value of k_s for aluminum is 0.3, Hooputra et al. (2004), while here k_s is set equal to 0.5. The law chosen for $\bar{\varepsilon}_S^{pl}$ as a function of θ_S is illustrated in Fig. 8. During the FE calculation, the criterion for damage initiation is met when a condition of the same form of Eq. (6) is satisfied. After the onset of damage, a damage evolution law of the same type of that assumed for the ductile phase is followed, tuned with the parameters reported in Tab. 5.

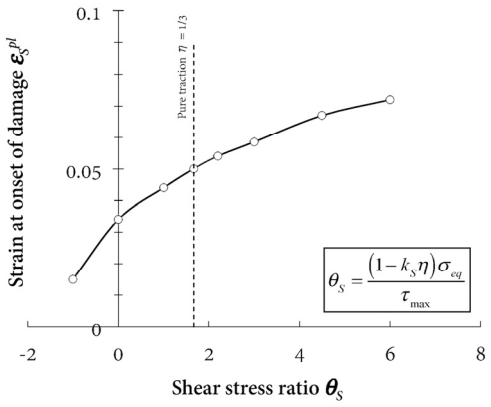

Fig. 8. Equivalent strain at the onset of damage for pearlite.

5. Results and discussion

5.1. Elastic properties and size verification of the RVEs

Elastic properties of the RVEs are analyzed calculating the engineering constants on the three directions corresponding to the cartesian reference system axes, which are reported in Tab. 6. Resulting density is also reported. Elasticity modules are close to the experimental ones with a maximum difference of 5% and variation between the three directions are within 2%. This result confirms that the chosen size of the RVE is acceptable. From the results of elastic properties calculation it is possible to extract also the maximum stress concentration factors exerted by the voids population along the 3 directions, namely K_{t1}, K_{t2} and K_{t3}. On the RVEs these have values varying between 2 and 2.6, which are higher that the single spherical void solution ($K_t = 2$) because of voids interaction effect. Analyzing the results in the work by Bidhar et al. (2011) for paired spherical cavities, the RVEs behave as if they contain an average distance between the nodules (hera treated as cavities only) of about 1.2/1.3 times the nodule diameter. Here nodules do not have the same diameter, however entering this value in Eq. (1) would give a local matrix triaxiality estimation of (1/3 + 0.25) ≈ 0.6. As shown in the following paragraph 5.3, triaxiality developed in the RVE is locally much higher.

Table 6. Homogeneous elastic properties of RVEs (in GPa).

RVE	E_{11}	E_{22}	E_{33}	G_{12}	G_{13}	G_{23}	ν_{12}	ν_{13}	ν_{23}	ρ (kg/m^3)	K_{t1}	K_{t2}	K_{t3}
M1	163.6	166.0	165.2	63.6	63.8	64.4	0.283	0.286	0.289	6.92	2.24	2.36	2.18
M2	167.1	167.1	167.0	64.9	65.0	65.0	0.287	0.288	0.288	6.98	2.18	2.08	2.02
M3	179.6	179.5	179.6	69.1	69.1	69.1	0.291	0.291	0.291	7.23	2.24	2.17	2.56

5.2. Tensile response

Tensile response of the RVEs is obtained by plotting the resulting nominal meso-stress Σ_{11} vs. the imposed elongation E_{11}. The resulting curves, plotted in Fig. 9, show a very good agreement with experimental tensile responses taken from Nicoletto et al. (2002) and Collini et al. (2005). Elasticity, onset of plasticity and strain hardening are correctly described by the simulations. Regarding the failure strain, it can be seen that the data of Tab. 5 for the damage models described in sections 4.3 and 4.4 represent correctly tuned in terms of the mesh-dependent plastic displacement at failure $\dot{\bar{u}}^{pl} = L_{EL}\dot{\bar{\varepsilon}}^{pl}$ with. Simulations are interrupted when the element deletion feature makes the time increment falling under 10^{-5}, because of loss of convergence of the finite element solution.

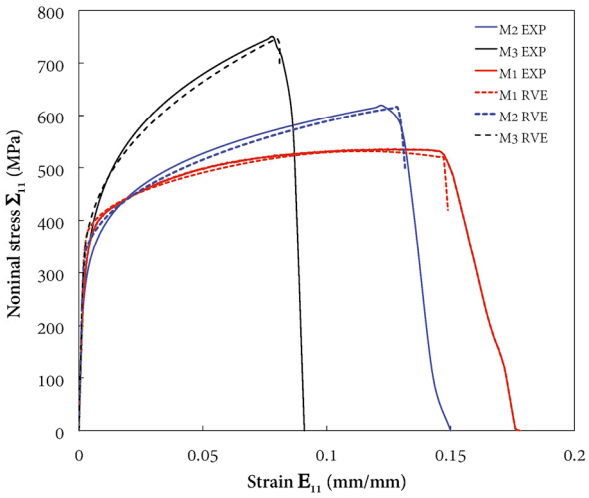

Fig. 9. Tensile curves of RVEs and experiments.

5.3. Strain distribution, triaxiality and damage initiation

Maps of plastic strain, triaxiality and damage variables are illustrated in the cut-out contours of Fig. 10, obtained for a constant far-field applied stress and $T = 1/3$ along direction 1. It can be noticed that plastic strain looks extremely inhomogeneous, concentrating around the nodules. Ferritic microstructure M1 leaves more inter-particle space where shear strain develops easily. However, for mixed structures higher equivalent stresses with lower equivalent plastic strains are present in the pearlite with respect to the ferrite. With this strains and stress triaxiality distribution in the matrix, critical damage is attained in the pearlite before than the ferrite. Local triaxiality in the matrix obvously differs greatly from the one imposed at the mesoscale for all the investigated range $-1/3 < T < 5/3$.

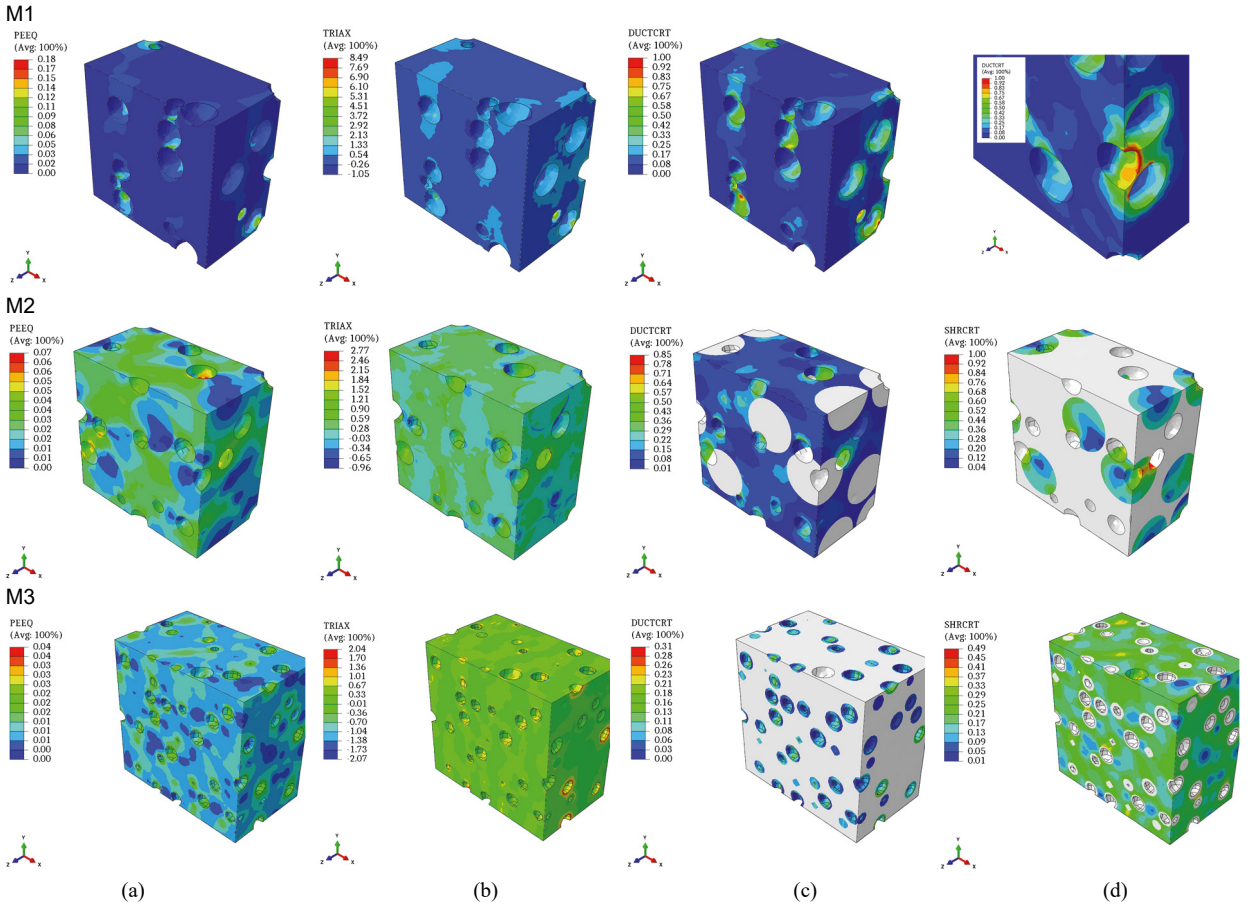

Fig. 10. Equivalent plastic strain (a), local stress triaxiality (b), ductile (c) and shear (d) damage variables in the M1, M2, M3 microstructures at failure under $T = 1/3$.

5.4. Strain to failure

The plot of Fig. 11 summarizes the resulting RVE strain to failure data as calculated from Eq. (4), over the imposed triaxiality range. Ferritic matrix DCI (red dots) fails following the ferrite failure behavior, just lowered in terms of strain by the voids action in concentrating the strain and increasing the local triaxiality with respect to homogeneous ferrite. As previously seen from experiments, graphite nodules play a double role in decreasing the ductility of the matrix, since they concentrate the plastic strain and confine the strain itself creating local higher hydrostatic pressure. The few available experimental data on failure of GJS-400 spheroidal ductile iron at different triaxialities, Memhard et al. (2011), follow the trend predicted by the RVE model.

The mixed ferritic/pearlitic structures exhibit a dual behavior, which depends on T. A local maximum of failure strain is found nearby the tensile loading condition, and an increasing trend for negative triaxialities. This peculiar behavior resembles that found by Bao and Wierzbicki (2004) on 2024-T351 aluminum alloy and in Bai et al. (2009) on 1045 and DH36 steels, which are explained in terms of two-parameter (triaxiality and Lode angle) dependence, see Bao and Wierzbicki (2008). In fact, also the shear damage model used here for the pearlite is a two-parameter model that, with parameters identified on unixial tensile DCI tests (Tab. 5) yields on the mesoscale a decrease of failure strain with decreasing triaxiality. However, no data about strain to failure as function of stress triaxiality have been retrieved for pearlitic-ferritic DCIs, therefore the behavior predicted by the RVE has still to be proven experimentally in this case.

A deeper analysis of the damage initiation and evolution in the phases during the traction loading confirms that the shear damage variable ω_S describing the pearlite, increases before and faster than the ductile damage variable ω_D. This can be easily detected from the plot of Fig. 12 where the RVEs are subject to a uniform traction Σ_{11}.

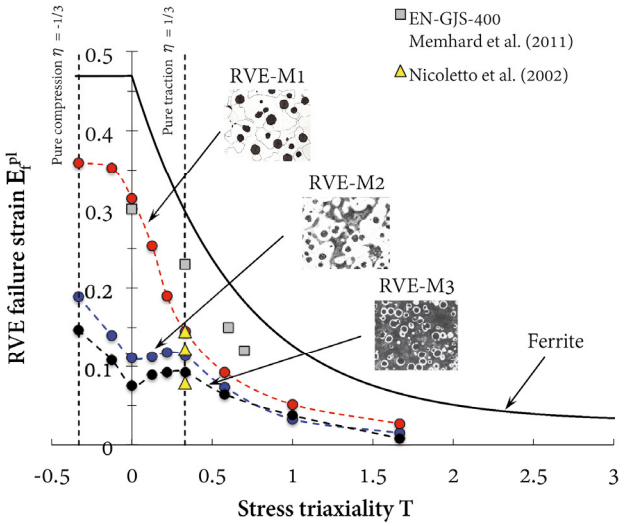

Fig. 11. Failure strains vs. imposed triaxiality at the RVE.

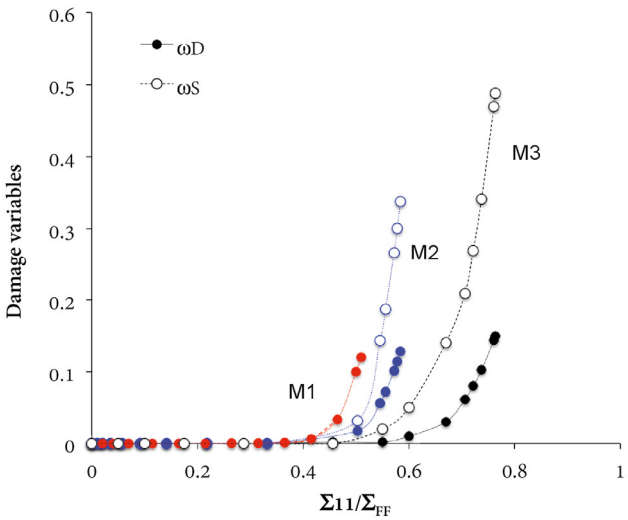

Fig. 12. Damage variables during elongation at imposed $T = 1/3$.

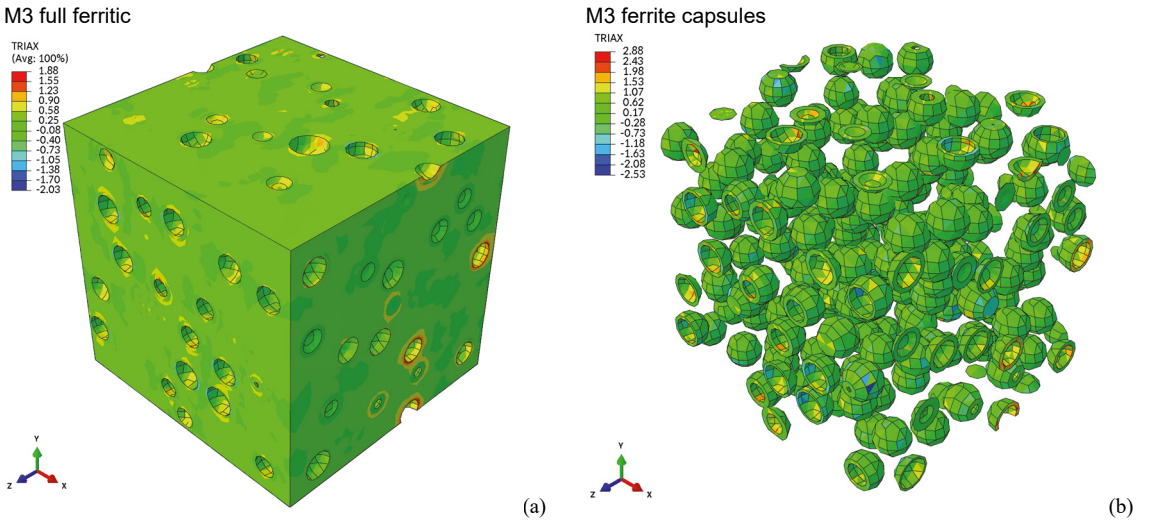

Fig. 13. Local triaxiality in the ferrite at $T = 1/3$ and $E_{11} = 5\%$ for RVE M3, full ferritic (a) and ferritic/pearlitic with the bull's eye structure (b).

Finally, the analysis of local triaxiality in the ferritic capsules of the nearly full pearlitic structure put a light on the ambiguous behavior of ferrite that results in local cleavage fracture under certain circumstances (see Sect. 2.1). For the sake of comparison, the original mixed structure M3 and a full ferritic M3 volume, namely M3-F, is run and tested under strain controlled condition, $E_{11} = 5\%$.

Results, summarized in Tab. 7, reveal a net contribution of the constraint of pearlite on ferrite capsules and a local increasing of about 50% on η that decrease strongly their local plastic strain to failure.

Table 7. Analysis of the behavior of ferrite under strain controlled test $E_{11} = 5\%$

RVE		σ_{eq} (MPa)	ε_{PEEQ}	η	ω_D or ω_S
M3-F	Ferrite	644	$3.1 \cdot 10^{-2}$	1.88	0.09
M3	Ferrite capsules	653	$3.6 \cdot 10^{-2}$	2.88	0.11
	Pearlite	851	$1.9 \cdot 10^{-2}$	1.98	0.48

6. Conclusions

In this work 3-D periodic RVEs are generated with the aim of modeling the failure strain of ferritic/pearlitic ductile cast iron microstructures. Different failure models that depend on local triaxiality are used to describe the behavior of the single constituents at the microscale, while various triaxialities are imposed to the RVE boundaries at the mesoscale.

From the analysis of results, the main conclusions can be summarized as follows:

- The periodic random RVE approach is a powerful tool to obtain information at the meso-scale starting from local description of constituents, and to zoom back to the behavior at the microscale;
- DCI microstructures show that due to heterogeneity, plastic strain localization and interaction of voids, local triaxialities that are considerably different from that imposed at the mesoscale are developed;
- mixed ferrite/pearlite microstructures show a competition of damage mechanism, exhibiting the maximum of failure strain at $\eta \approx 0.25$;
- in almost fully pearlitic structures, where nodules are smaller and closer, encapsulated ferrite can be subjected to extremely high triaxiality that promotes the cleavage fracture.

References

Andriollo T., Zhang Y., Fæster S., Thorborg J., Hattel J. Impact of micro-scale residual stress on in-situ tensile testing of ductile cast iron: Digital volume correlation vs. model with fully resolved microstructure vs. periodic unit cell. Journal of the Mechanics and Physics of Solids 2019;125:714–735.

Bai Y., Teng X., Wierzbicki T. On the application of stress triaxiality formula for plane strain fracture testing. Journal of Engineering Materials and Technology 2009;131:021002-2.

Bai Y., Wierzbicki T. A new model of metal plasticity and fracture with pressure and Lode dependence. International Journal of Plasticity 2008;24:1071–1096.

Bao Y., Wierzbicki T. On fracture locus in the equivalent strain and stress triaxiality space. International Journal of Mechanical Sciences 2004;46:81–98.

Berdin C., Dong M.J., Prioul C. Local approach of damage and fracture toughness for nodular cast iron. Engineering Fracture Mechanics 2001;68:1107–1117.

Bidhar S., Kuwazuru O., Hangai Y. , Yano T., Utsunomiya T., Yoshikawa N. Empirical prediction of stress concentration factor for a pair of spherical cavities. Fourth International Conference on Modeling, Simulation and Applied Optimization – Kuala Lumpur (Malaysia) 2011.

Bonora N., Ruggiero A. Micromechanical modeling of ductile cast iron incorporating damage. Part I: Ferritic ductile cast iron. International Journal of Solids and Structures 2005;42:1401–1424.

Bradley W.L., Srinivasan M.N. Fracture and fracture toughness of cast irons. International materials review 1990;35(3)

Chao C.G., Lui T.S., Hon M.H. The effect of triaxial stress field on intermediate temperature embrittlement of ferritic spheroidal graphite cast irons. Metallurgical Transactions A 1988;19:1213–1219.

Cheng G., Hu X.H., Choi K.S., Sun X. Predicting grid-size-dependent fracture strains of DP980 with a microstructure-based post-necking model. International Journal of Fracture 2017;207(2):211–227.

Collini L. La modellazione microstrutturale di materiali a struttura eterogenea: princìpi ed applicazioni. Frattura e Integrità Strutturale. 2010;12:21–36.

Collini L., Nicoletto G. Determination of the relationship between microstructure and constitutive behavior of nodular cast iron with a unit cell model. Journal of Strain Analysis for Engineering Design 2005;40(2):107–116.

Dahlberg C.F., Öberg M., Faleskog J. Continuum modeling of nodular cast iron using a porous plastic model with pressure-sensitive matrix – experiments, model calibration & verification. Tech rep KTH Royal Institute of Technology, School of Engineering Science – Stockholm (Sweden), 2014.

Davis, J.R. (Ed.) ASM Specialty Handbook – Cast Irons. ASM International, Metals Park, Ohio, 1996.

Di Cocco V., Iacoviello F., Rossi A. Cavallini M. Stress triaxiality influence on damaging micromechanisms in a pearlitic ductile cast iron. Frattura ed Integrità Strutturale 2014;30:462–468.

Di Cocco V., Iacoviello F., Rossi A., D., Cavallini M., Natali S. Analysis of stress triaxiality influence: ferritic DCI damaging micromechanisms Acta Fracturae – Rome (Italy), 2013.

Di Cocco V., Iacoviello F., Rossi A., Iacoviello D. Macro and microscopical approach to the damaging micromechanisms analysis in a ferritic ductile cast iron. Theoretical and Applied Fracture Mechanics 2014;69:26–33.

Dollar M., Bernstein I.M., Thompson A.W. Influence of deformation substructure on flow and fracture of fully pearlitic steel. Acta Metall. 1988;36:311–320.

Dong M.J., Prioul C., François D. Damage effect on the fracture toughness of nodular cast iron: Part I. Damage characterization and plastic flow stress modeling. Metall. Mater. Trans. A 1997;28A:2245–2254.

Endo M., Yanase K. Effects of small defects, matrix structures and loading conditions on the fatigue strength of ductile cast irons. Theor Appl Fract Mech 2014;69:34–43.

Gensamer M., Pearsall E.B., Pellini W.S., Low J.R.The Tensile Properties of Pearlite, Bainite, and Spheroidite Metallogr. Microstruct. Anal. 2012;1:171–189.

Ghahremaninezhad A., Ravi-Chandar K. Deformation and failure in nodular cast iron Acta Materialia 2012;60:2359–2368.

Gonzaga R.A., Martínez Landa P., Perez A., Villanueva P. Mechanical properties dependency of the pearlite content of ductile irons. Journal of Achievements in Materials and Manufacturing Engineering 2009;33/2:150–158.

Guillermer-Neel C., Feaugas X., Clavel M. Mechanical behavior and damage kinetics in nodular cast iron: Part I. Damage mechanisms. Metall. Mater. Trans. A 2000;31A:3063–3074.

Hancock J.W., Mackenzie A.C. On the mechanisms of ductile failure in high-strength steels subjected to multi-axial stress-states. Journal of the Mechanics and Physics of Solids 1976;24:147–169.

Hohenwarter A., Kapp M.W., Völker B., Renk O., Pippan R. Strength and ductility of heavily deformed pearlitic microstructures IOP Conf. Series: Materials Science and Engineering 2017;219:012003.

Hooputra H., Gese H., Dell H., Werner H. A comprehensive failure model for crashworthiness simulation of aluminium extrusions. International Journal of Crashworthiness 2004;9(5):449–464.

Hopperstad O.S., Børvik T., Langseth M., Labibes K., Albertini C. On the influence of stress triaxiality and strain rate on the behaviour of a structural steel. Part I. Experiments. European Journal of Mechanics A/Solids 2003;22:1–13.

Hradil P., Talja A. Ductility limits of high strength steels. Research report VTT-R-04741-16, 2017. FIMECC Research Portal and VTT webpage.

Hütter G., Zybell L., Kuna M. Micromechanisms of fracture in nodular cast iron: From experimental findings towards modeling strategies – A review. Engineering Fracture Mechanics 2015;144:118–141.

Hyzak J.M., Bernstein I.M. The role of microstructure on the strength and toughness of fully pearlitic steels. Metallurgical Transactions A 1976;7(8):1217–1224.
Iacoviello F., Di Bartolomeo O., Di Cocco V., V. Piacente V. Damaging micromechanisms in ferritic–pearlitic ductile cast irons. Materials Science and Engineering 2008;A478:181–186.
Iacoviello F., Di Cocco V., Rossi A., Cavallini M. Ferritic-pearlitic ductile cast irons: is ΔK a useful parameter? 13th International Conference on Fracture – Beijing (China), 2013.
Johnson G.R., Cook W.H. Fracture characteristics of three metals subjected to various strains, strain rates, temperatures and pressures. Engineering Fracture Mechanics 1985;21(1):31–48.
Kanita T., Foresta S., Gallieta I., Mounourya V., Jeulin D. Determination of the size of the representative volume element for random composites: statistical and numerical approach. International Journal of Solids and Structures 2003;40(13-14):3647–3679.
Kobayashi T. Ductile cast iron. In: Strength and toughness of materials. Springer; 2004. p. 89–110.
Kuna M., Sun D.-Z. Analysis of void growth and coalescence in cast iron by cell models. J. de Physique IV 1996;6(C6):113–122.
Lacaze J., Sertucha, J., Åberg L.M. Microstructure of as-cast ferritic-pearlitic nodular cast irons. ISIJ International, 2016;56(9):1606–1615.
Lewandowski J.L., Thompson A.W. Microstructural effects on the cleavage fracture stress of fully pearlitic eutectoid steel. Metallurgical and Materials Transactions A 1986;17(10):1769–1786.
Lin R.C., Steglich D., W. Brocks W., Betten J. Performing RVE calculations under constant stress triaxiality for monotonous and cyclic loadingInt. J. Numer. Meth. Engng 2006;66:1331–1360.
Lin Y.F., Lui T.S., L. H. Chen. The effect of triaxial stress on ductility and fracture morphology of ferritic spheroidal graphite cast iron. Metallurgical and Materials Transactions A 1994;25(4): 821–825.
Liu M.M., Chen J.J. Micromechanical analysis on the failure criterion of ductile material. Procedia Engineering 2015;130:1097–1104.
Manjoine M.J. Creep-rupture behavior of weldments. Welding Research Supplement 1982:50s–57s.
Maresca G., Milella P.P., Pino G. A critical review of triaxiality based failure criteria. Procs. of IGF 13 – Cassino (Italy), 1997.
Memhard D., Andrieux F., Sun D.-Z., Häcker R. Development and verification of a material model for prediction of containment safety of exhaust turbochargers. In: 8th European LS-DYNA users conference; 2011.
Miller L.E., Smith G.C. Tensile fractures in carbon steels. J. Iron Steel Inst. 1970;208:998–1005.
Mirza M.S., Barton D.C., Church, P. The effect of stress triaxiality and strain-rate on the fracture characteristics of ductile materials. J. Materials Sci. 1996;31:453–461.
Needleman A. Continuum model for void nucleation by inclusion debonding. Journal of Applied Mechanics 1987;54:525–531.
Needleman A., Tvergaard, V. An analysis of dynamic, ductile crack growth in a double edge cracked specimen. International Journal of Fracture 1991;49:41–67.
Nemoto Y., Shibanuma K., Suzuki K., Sadamatsu S., Adachi Y., Aihara S. 3D observation of micro-cracks as cleavage fracture initiation site in ferrite-pearlite steel. ISIJ International 2017;57(4): 746–754.
Nicoletto G., Collini L., Konecna R., Bujnova P. Damage mechanism in ferritic-pearlitic nodular cast iron. Transactions of Famena. 2004;28(2):19–26.
Nicoletto G., Collini L., Konecna R., Riva E. Analysis of nodular cast iron microstructures for micromechanical model development. Strain 2006;42(2):89–96.
Nicoletto G., Konecna R., Hadzimova B., L. Collini L. Microstructure and mechanical strength of nodular cast irons. Procs. of AIAS Conference – Parma (Italy), 2002.
Ohata M., Suzuki M., Ui A., Minami F. 3D-Simulation of ductile cracking in two-phase structural steel with heterogeneous microstructure. 17th European Conference on Fracture – Brno (Czech Republic), 2008.
Omairey S.L., Dunning P.D., Sriramula S. Development of an ABAQUS plugin tool for periodic RVE homogenisation. Engineering with Computers 2019;35(2):567–577.
Peng X., Pi W., Fan J. A microstructure-damage-based description for the size effect of the constitutive behavior of pearlitic steels. International Journal of Damage Mechanics 2010;19:821–849.
Richter H. Mote3D: an open-source toolbox for modelling periodic random particulate microstructures. Modelling Simul. Mater. Sci. Eng. 2017;25(3):035011
Springer H.K. Mechanical characterization of nodular ductile iron. Rep. LLNL-TR-522091, 2012.
Steglich, D., Brocks B. Micromechanical modelling of the behaviour of ductile materials including particles. Computational Materials Science 1997;9:7–17.
Tartaglia M., Ritter P.E., Gundlach R.B. DIS Ductile Iron Society, Research project No. 30, 2000.
Toribio J., Ayaso F.J., Micro-fracture maps in progressively drawn pearlitic steels under triaxial stress states. International Journal of Materials Engineering Innovation 2009;1(1):61–73.
Toribio J., González B., Matos J.-C., Ayaso F.-J. Influence of microstructure on strength and ductility in fully pearlitic steels. Metals 2016;6: 318.
Tvergaard, V. Effect of void size difference on growth and cavitation instabilities. J. Mech. Phys. Solids 1996;44(8), 1237–1253.
Voigt R.C., Eldoky L.M., Chiou H.S. Fracture of ductile cast irons with dual matrix structure. AFS Trans. 1986;94:645–656.
Yanagisawa O., T.S. Lui T.S. Influence of the structure on the 673 K embrittlement of ferritic spheroidal graphite cast iron. Transactionosf the Japan Institute of Metals 1983; 24(12):858–867.
Zhang K.S., Bai J.B., François D. Ductile fracture of materials with high void volume fraction. Int J Solids Struct 1999;36(23):3407–25.
Zybell L., Hütter G., Linse T., Mühlich U., Kuna M. Size effects in ductile failure of porous materials containing two populations of voids. Eur J Mech A – Solid 2014;45:8–19.